Designing topological and correlated 2D magnetic states via superatomic lattice constructions of zirconium dichloride

Yang Song[1,§], Wen-Han Dong[2,3,§], Kuan-Rong Hao[1], Shixuan Du[2], and Lizhi Zhang[1] (✉)

[1] *Laboratory of Theoretical and Computational Nanoscience, National Center for Nanoscience and Technology, Beijing 100190, China*
[2] *Beijing National Laboratory for Condensed Matter Physics and Institute of Physics, Chinese Academy of Sciences, Beijing 100190, China*
[3] *State Key Laboratory of Low Dimensional Quantum Physics and Department of Physics, Tsinghua University, Beijing 100084, China*
[§] *Yang Song and Wen-Han Dong contributed equally to this work.*

ABSTRACT

Magnetic materials could realize the intriguing quantum anomalous Hall effect and metal-to-insulator transition when combined with band topology or electronic correlation, which have broad prospects in quantum information, spintronics, and valleytronics. Here, we propose the approach of designing novel two-dimensional (2D) magnetic states via *d*-orbital-based superatomic lattices. Specifically, we chose triangular zirconium dichloride disks as superatoms to construct the honeycomb superatomic lattices. Using first-principles calculations, we identified a series of 2D magnetic states with varying sizes of superatoms. We found the non-uniform stoichiometries and geometric effect of superatomic lattice give rise to spin-polarized charges arranged in different magnetic configurations, containing ferromagnetic coloring triangles, antiferromagnetic honeycomb, and ferromagnetic kagome lattices. Attractively, these magnetic states are endowed with nontrivial band topology or strong correlation, forming an ideal Chern insulator or antiferromagnetic Dirac Mott insulator. Our work not only reveals the potential of *d*-orbital-based superatoms for generating unusual magnetic configurations, but also supplies a new avenue for material engineering at the nanoscale.

KEYWORDS

topological state, Chern insulator, Dirac Mott insulator, zirconium dichloride, superatomic lattice, kagome lattice

1   Introduction

Magnetic and topological quantum states have attracted extensive research interests in condensed matter physics and material science [1–4]. Recent studies of layered materials uncovered a wide spectrum of long-range magnetic orders, including intralayer ferromagnetic (FM) CrI_3 [5] and Fe_3GeTe_2 [6], interlayer antiferromagnetic (AFM) $FeCl_2/FeBr_2$ [7], etc. These two-dimensional (2D) magnetic layers offered great chances for device functionalities, e.g., electrical control of magnetic states [8]. In addition, topological states were originally proposed in nonmagnetic systems [9, 10]. The bulk band topology gives rise to exotic phenomena, such as robust bulk-boundary correspondence and nondissipative transport properties in topological insulators (TIs) and topological semimetals [11–16]. The combination of magnetism and topology is known as a magnetic topological state, and magnetism offers more freedom to manipulate topological states [17–22]. But it also creates challenges for both theoretical prediction and experimental characterization of magnetic topological materials due to much more complicated electronic interactions than nonmagnetic materials [23]. The breakthrough of magnetic TI happened in 2019, during which the AFM TI and axion insulator states were predicted and observed in the $MnBi_2Te_4$ family [21, 24]. After that, the high-throughput method was used to screen out magnetic topological materials [17, 19]. Various topological quantum effects have been discovered in

experiments. Examples include the quantum anomalous Hall effect (QAHE) observed in thin films of chromium-doped (Bi, Sb)$_2$Te$_3$ [25] and intrinsic magnetic TI $MnBi_2Te_4$ [26], and giant anomalous Nernst effect caused by Berry curvature in FM semimetal Co_2MnGa [27].

On the other hand, the magnetic systems are favorable for strong electronic correlations except for band topology. A well-known example is the AFM kagome lattice, which may host both frustrated magnetic order and nontrivial topology [28, 29]. A recent study has shown that electron correlation can drive 1T-TaS_2 into the kagome Mott insulator described by Kagome–Hubbard models [30]. For graphene-like honeycomb lattice, the interaction-driven Dirac Mott insulator is appealing to the researchers of 2D materials because of the AFM-induced (semi)metal-to-insulator transition [31, 32]. Specifically, the Dirac Mott insulator displays a semimetallic phase with the Dirac cone at the Fermi level in its nonmagnetic configuration, and it appears as an insulating phase in the AFM ground state. Monte Carlo simulations have shown the phase diagram for the Hubbard model on the honeycomb lattice that the system first enters into the disordered spin liquid state when $3.5 < U/t < 4.3$, then ends into an AFM Mott insulator when $U/t > 4.3$ [32]. Here, U is the on-site Coulomb repulsion between two electrons with the opposite spins and t is the nearest-neighbor inter-site coupling between two electrons with the same spin. Based on this criterion, several Dirac Mott insulators are

---

proposed in carbon-based systems [33, 34]. Without exception, these Dirac Mott insulators possess a honeycomb superatomic lattice, in which the superatoms are carbon-skeleton flakes. Recently, some transition-metal-based superatomic lattices have also been synthesized in experiment [35]. It is worth mentioning that the circular dichroism Hall effect of Dirac Mott insulator was proposed, where the Hall effect can be activated at both K and K' valleys, and the direction of transversal Hall current can be controlled by circularly polarized light [34]. To date, the reported Dirac Mott insulators have been very limited, and more Dirac Mott insulators need to be designed for exotic valleytronic effects like the circular dichroism Hall effect.

Here, based on first-principles calculations, we designed and discovered both the Chern insulator and AFM Dirac Mott insulator in different sized 2D superatomic lattices of zirconium dichloride ($ZrCl_2$). The superlattices are named as SL*N*, where *N* is the number of rows of Zr atoms. It is worth noting that single crystal $ZrCl_2$ has been synthesized by mixing ZrCl and $ZrCl_4$ powders and substantially heating [36]. In the designed structures, the triangular $ZrCl_2$ disks act as superatoms of the honeycomb lattice. The stoichiometric ratio at the edges ($ZrCl_3$) is different from that of the disk centers ($ZrCl_2$), resulting in the non-uniform spatial distributions of spin charges. The spin charges form various equivalent magnetic lattices in different sized superatomic lattices, containing FM coloring triangle (CT) [37], AFM honeycomb, and FM kagome lattice. The non-zero Chern numbers of $C = 1$ demonstrate that FM CT and FM kagome lattices are Chern insulators. The AFM honeycomb lattice satisfies the criterion of $U/t = 10.6 > 4.3$, indicating a Mott insulator. In summary, diverse topological and correlated magnetic states have been designed via the *d*-orbital-based 2D honeycomb superatomic lattice with different sizes. This work provides a new pathway for designing novel magnetic materials.

2   Methods

Density functional theory (DFT) calculations were implemented in the Vienna *ab initio* simulation package (VASP) [38, 39] using the projector-augmented wave (PAW) method combined with the Perdew–Burke–Ernzerhof (PBE) [40] functional. The in-plane lattice constants of SL2, SL3, and SL4 were 12.31, 20.19, and 26.93 Å, respectively. The vacuum layers for all unit cells were larger than 20 Å. The atoms were fully relaxed until the force on each atom was less than 0.01 eV·Å^{-1}. The plane-wave basis was set to an energy cutoff of 500 eV. The Brillouin zone was sampled by Gamma-centered *k*-meshes [41] of ($6 \times 6 \times 1$) for SL2, ($5 \times 5 \times 1$) for SL3, and ($4 \times 4 \times 1$) for SL4, respectively. For SL2, we constructed maximally localized Wannier functions using *d* orbitals of Zr atoms via Wannier90 code [42]. The edge spectrum was calculated by the iterative Green's function technique [43], as implemented in the WannierTools package [44].

To verify the dynamical stability of SLs, phonon dispersion calculations were performed by using the density functional perturbation theory [45, 46], as implemented in the Phonopy code [47] that interfaced with VASP. Considering the large sizes of the unit cells of SLs (12.3, 20.2, and 26.9 Å), we applied the 2×2 supercells for SL2/SL3 and a 1×1 unit cell for SL4 to keep a balance between computational efficiency and accuracy. The convergence criterion for energy was 10^{-6} eV. The *ab initio* molecular dynamics (AIMD) simulations were carried out using a canonical (NVT) ensemble [48]. The time interval for each AIMD step was 2 fs. The formation energies in the convex hull diagram were calculated under the magnetic ground states of Zr_mCl_n.

3   Results and discussion

As shown in Fig. 1(a), we designed a series of honeycomb superatomic lattices, where each superatom (marked by a black dotted circle) was a triangular disk of $ZrCl_2$ (backgrounded by light blue) whose edges could be considered as $ZrCl_3$ in stoichiometry (backgrounded by light yellow). The blue and green balls denote Zr and Cl atoms, respectively. Monolayer $ZrCl_2$ with space group $P\bar{6}m2$ (No. 187) is nonmagnetic [49, 50] (see Fig. 1(b)), while monolayer $ZrCl_3$ with space group $P\bar{6}2m$ (No. 189) is FM [51] (see Fig. 1(c)). Both of them possess a sandwich-like structure with Cl atoms on the top and bottom surfaces and Zr atoms in the middle. Figure 1(a) shows the unit cell for $ZrCl_2$ superatomic lattice. The size of the superatomic lattice is denoted by *N*, i.e., the number of rows of Zr atoms in a superatom, outlined by red dashed lines. For example, *N* is equal to three in Fig. 1(a). Here, we focus on the superatomic lattices SL2, SL3, and SL4. When *N* is equal to one, the superatomic lattice degenerates
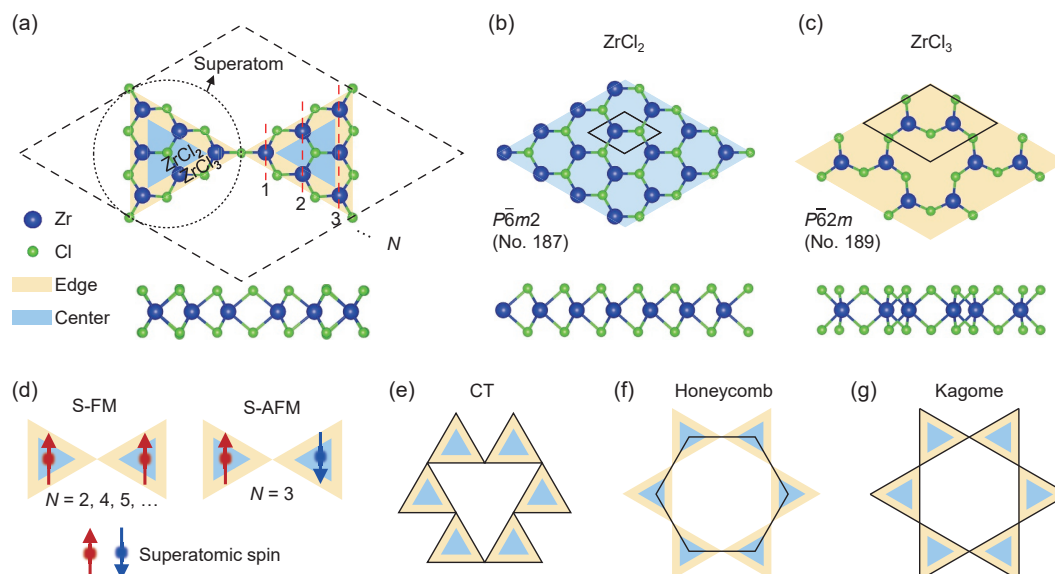

Figure 1 Atomic structures and different superatomic spin-polarized lattices formed by $ZrCl_2$ disks. (a) Superatomic lattice with $ZrCl_2$ composition in the center (marked by light blue) and $ZrCl_3$ composition at the edge (marked by light yellow). The blue and green balls are Zr and Cl atoms, respectively. *N* is the number of rows of Zr atoms in a superatom. The top and side views for (b) monolayer $ZrCl_2$ and (c) monolayer $ZrCl_3$, respectively. (d) Schematic diagrams of S-FM and S-AFM. The red and blue arrows denote superatomic spin-up and spin-down. Equivalent superatomic spin lattices, such as (e) CT, (f) honeycomb, and (g) kagome lattices.

into monolayer $ZrCl_3$. It is noted that the non-uniform stoichiometries between the centers and edges of the superatoms naturally result in the internal distributions of spin-polarized charges. Each $ZrCl_2$ superatom as a whole hosts a magnetic moment of 1 μ_B. As shown in Fig. 1(d), the superatom can arrange in superatomic FM (S-FM) or AFM (S-AFM) configurations, where the red and blue arrows denote the superatomic spin-up and spin-down. Our work shows that superatomic lattices possess different magnetic ground states. It is S-FM for SL2 and SL4, but S-AFM for SL3. One significant difference between superatomic spin and atomic spin is that the former has internal spin charge distributions according to the geometric effect, thus the equivalent magnetic configurations go beyond honeycomb lattice. The geometric effect means that Zr atoms at the centers and edges are different, thus the spin polarized charges are prone to gather at either the centers or linkages of two superatoms. It is interesting that we found three types of superatomic spin-rearranged lattices, containing CT, honeycomb, and kagome lattices (see Figs. 1(e)–1(g)). Different sized $ZrCl_2$ superatomic lattices possess different magnetic configurations and equivalent spin-polarized lattices. We will discuss the details in the sections below.

First, we focused on the smallest $ZrCl_2$ superatomic lattice, namely SL2. Figure 2(a) shows the distortion process from a kagome lattice to a CT lattice, which occurs in SL2. Figure 2(b) shows the top and side views of the atomic structure of SL2, whose chemical formula is Zr_6Cl_{18} and the space group is $P\bar{6}2m$ (No. 189). Notice the spin-polarized charges mainly centered at the linkages of superatoms forming a distorted kagome lattice, i.e., a CT alike lattice marked by black dashed lines. Figure 2(c) illustrates that the distorted structure is the energetically favorable ground state. The distorted structures of SL2 exist under a wide range of biaxial strains. Such distortion of SL2 resembles the structure of monolayer $ZrCl_3$ in Fig. 1(c), because the superatoms are small and their linkages are flexible. Our calculations reveal the FM state is the ground state, lower than the nonmagnetic (NM) state by 125.69 meV per unit cell. The FM band structure of SL2 is

shown in Fig. 2(d). One can clearly see the typical three-band characteristics from CT lattice, i.e., kagome-like bands in one spin channel [37]. In particular, the bands split into two groups of three bands with opposite spins due to the superatomic magnetic exchange. The orange solid and blue dashed lines denote the spin-up and spin-down electronic bands, respectively. The spin-up three bands are composed of two Dirac bands and one topological flat band. The Dirac cone appears exactly at the Fermi level, with the lower two bands filled. Therefore, the total magnetic moment in one unit cell is 2 μ_B. It means each superatom contributes a magnetic moment of 1 μ_B, and the FM state is actually an S-FM. The FM band structure of SL2, including spin-orbit coupling (SOC), is also shown in the right inset of Fig. 2(d). A band gap of 3.4 meV opens at the Dirac point due to the SOC effect from Zr atoms, indicating the nature of intrinsic magnetic TI states. Figure 2(e) shows the spin-resolved projected density of states (PDOS) of SL2, where the electronic states around the Fermi level are dominated by d_{z^2}, d_{xy}, and $d_{x^2-y^2}$ orbitals of Zr atoms. The PDOS of d_{xy} and $d_{x^2-y^2}$ orbitals are degenerate, thus we used line and filled pattern to distinguish them. Moreover, we have calculated the Chern number (C) of SL2 in the S-FM state using Kubo formula [52], in which we obtained $C = 1$. In Fig. 2(f), the semi-infinite zigzag edge spectrum of SL2 shows that there is one chiral topological edge state which connects the valance band at K valley with the conduction band at K' valley, manifesting that SL2 is indeed a Chern insulator with $C = 1$. The chiral edge state means that SL2 is promising for superatomic quantum anomalous Hall devices with nondissipative transport.

Next, we investigated SL3, whose atomic structure is shown in Fig. 3(a). The chemical formula for SL3 is $Zr_{12}Cl_{34}$, with space group $P6/mmm$ (No. 191). We calculated the total energy of SL3 under NM, FM, and AFM states. The AFM state is the ground state, whose energy is lower than that of the FM and NM states by 5.2 and 76.1 meV per unit cell, respectively. The spin charge density differences ($\rho\uparrow - \rho\downarrow$) mainly distribute on the Zr atoms in the center of each superatom. The spin charge centers are
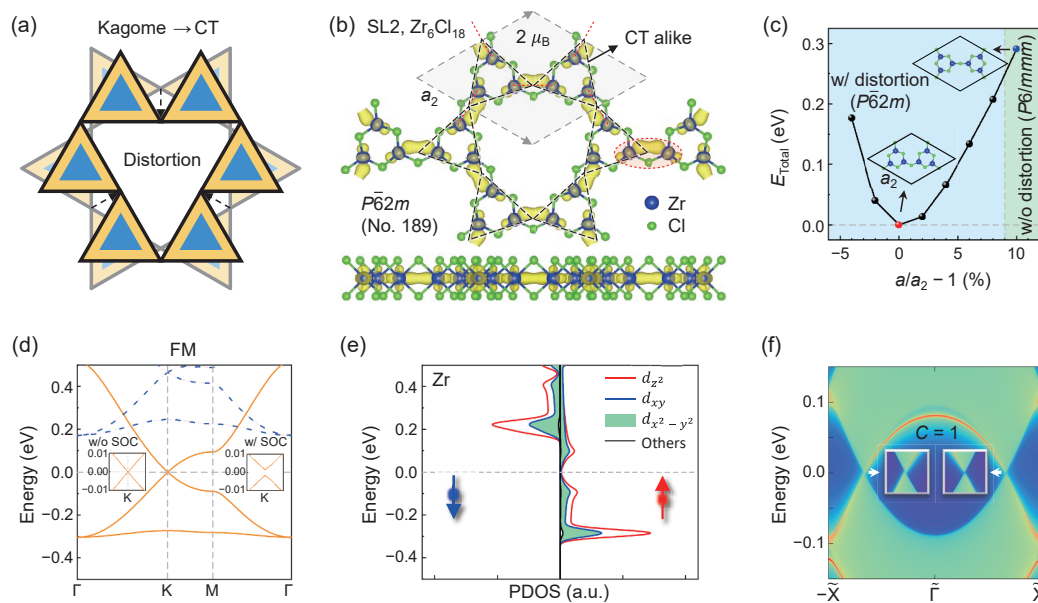

Figure 2 Atomic and electronic structures of SL2. (a) Schematic diagram of the distortion process from a kagome lattice to a CT lattice. (b) Atomic structure of distorted SL2 (formula Zr_6Cl_{18}) with spin charge density differences ($\rho\uparrow - \rho\downarrow$) forming into an FM CT alike lattice. The superatom is marked by black dashed lines. The unit cell is marked by gray rhombus. The lattice constant a_2 is 12.31 Å. The isosurfaces of spin-up $\Delta\rho\uparrow$ and spin-down $\Delta\rho\downarrow$ are marked by yellow and cyan, respectively. The isosurface level is chosen as 0.004 e·bohr^{-3}. The red semitransparent ellipse marks the spin-polarized charge centered at the linkage of two superatoms. (c) The relative total energies of SL2 under biaxial strains. The structures with and without distortion are marked by light blue and green backgrounds, respectively. The ground state (marked by red dot) is a distorted structure, as shown in the inset and (b). The blue dot denotes the relative total energy of SL2 under a tensile strain of 10%, which has no distortion. (d) Band structure of distorted SL2 in FM configuration. The orange solid and blue dashed lines denote the spin-up and spin-down bands, respectively. The insets show zoom-in band structures around the K point, without and with the SOC effect. (e) PDOS of Zr atoms projected on different d orbitals. (f) Semi-infinite zigzag edge spectrum of distorted SL2. The insets show there is one chiral edge state, indicating Chern number $C = 1$.

patterned into an AFM honeycomb lattice, as marked by black dashed lines in Fig. 3(a). Considering SL2 is a distorted structure, it is necessary to check if SL3 is distorted. The relative total energies for optimized structures under different biaxial strains were calculated and plotted in Fig. 3(b). The ground state highlighted by a red dot has no distortion, indicating the linkages of superatoms are rigid enough to avoid structure distortion. For comparison, the structural distortion appears when applying compressive biaxial strains. Figures 3(c)–3(e) show band structures of SL3 in NM, FM, and AFM states, respectively. For the NM configuration, the band structure shows the typical Dirac-band characteristics of a honeycomb lattice, whose Dirac cone locates at the K-point and at the Fermi level. For the FM configuration, the Dirac bands split into two groups with opposite spins due to the superatomic magnetic exchange. The spin-up Dirac bands are filled, indicating a total magnetic moment of $2\ \mu_B$. In the AFM configuration, an energy gap of 0.25 eV (E_g in Fig. 3(e)) opens because of the inversion symmetry breaking by long-range AFM order, which signifies a correlation-induced Dirac Mott insulating state [31].

To better understand such a Dirac Mott insulator state, we examined the phase diagram of correlated fermions in the graphene-like honeycomb lattice, as demonstrated in Ref. [32]. The magnetic ground state was determined by the U/t ratio of a standard Hubbard model, in which U denotes the on-site Coulomb repulsion between two electrons with the opposite spins, and t denotes the nearest-neighbor inter-site coupling between two electrons with the same spin. In the honeycomb lattice, AFM Mott insulating state is the ground state when $U/t > 4.3$. For SL3, we estimated U and t based on the method applied in Ref. [53]. Specifically, the electronic hopping strength t can be obtained from the NM state that $W = 6t$, where W is the bandwidth of Dirac bands. The strength of U corresponds to magnetic exchange caused by band splitting, which can be inferred from energy differences between the spin-up and spin-down bands at the K-point in the FM state. Here for the NM and FM states of SL3 in Figs. 3(c) and 3(d), we obtained $W = 0.17$ eV and $U = 0.30$ eV. The ratio of $U/t = 10.6$ confirms that the AFM Dirac Mott insulator state in Fig. 3(e) is caused by correlation-driven metal-to-insulator transition. Besides, we discovered that each superatom of SL3 carries exactly a spin-up or -down charge in the AFM state (see Fig. 3(a)), indicating an ideal S-AFM state. To distinguish from previous studies using carbon-based structures [33, 34], we highlight that SL3 extends the understanding of AFM Dirac insulators into d-orbital-based materials. As proposed in Ref. [34], SL3 is also promising for generating circular dichroism Hall effect and applying for valleytronic nanodevices.

In addition, we considered the larger superatomic lattice SL4, whose atomic structure is shown in Fig. 4(a). The chemical formula for SL4 is $Zr_{20}Cl_{54}$, sharing the same space group $P6/mmm$ (No. 191) with SL3. We found that the ground state of SL4 is FM, which is more energetically stable than the NM state by 101.84 meV. Its spin charge densities mainly distribute on the Zr atoms near the vertexes of the triangular superatoms. The spin charge centers are patterned into an FM kagome lattice. Similar to SL2, SL4 is arranged in an S-FM state, whose superatoms individually carry a magnetic moment of $1\ \mu_B$, while there is no structural distortion in SL4. Figure 4(b) shows the band structure for SL4 in the FM ground state. As expected, the typical three bands of kagome lattice appear. Akin to SL2 in Fig. 2(d), the bands are filled at the Dirac cone of the spin-up channel. The bandwidths of the three bands in SL2 and SL4 are 0.82 and 0.11 eV, respectively. The bandwidth decreases with the increase of superatom size, indicating that effective electronic coupling weakens with the increase of inter-superatomic distance. The decreased band dispersion is also consistent with the gradually increasing electron localization. It is obvious in Fig. 4(a) that the spin-polarized charges are inclined to locate at the linkages of superatoms. In addition, we calculated the Chern number of SL4. The obtained $C = 1$ indicates SL4 is a Chern insulator.
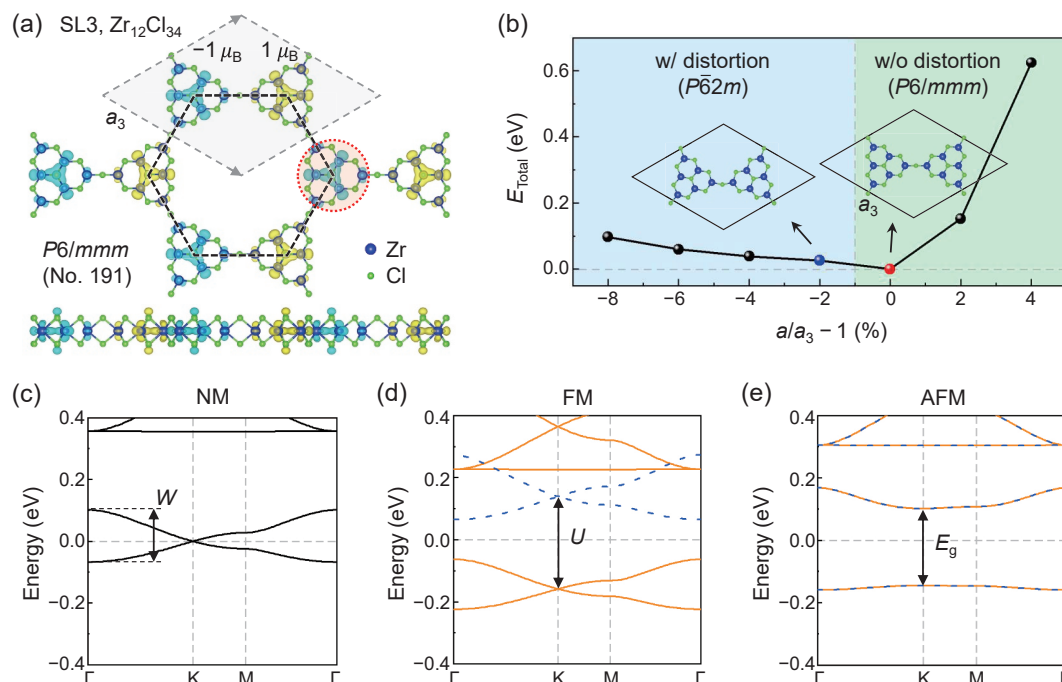

Figure 3 Atomic and electronic structures of SL3. (a) Atomic structure of SL3 (formula $Zr_{12}Cl_{34}$) with spin charge density differences ($\rho\uparrow - \rho\downarrow$) forming into an AFM honeycomb lattice, as marked by black dashed lines. The red semitransparent circle marks the spin charges around a charge center. The isosurfaces of spin-up $\Delta\rho\uparrow$ and spin-down $\Delta\rho\downarrow$ charge density are marked by yellow and cyan, respectively. The isosurface level is chosen as 0.002 e·bohr⁻³. The lattice constant a_3 is 20.19 Å. (b) The relative total energies of SL3 under different biaxial strains, compared with the ground state. The structures with and without distortion are marked by blue and green backgrounds, respectively. The structures of the ground state (marked by a red dot) and the state with a strain of −2% (marked by a blue dot) are shown in the insets. Band structures of SL3 in (c) NM, (d) FM, and (e) AFM configurations, respectively. In (d) and (e), the orange solid and blue dashed lines denote the spin-up and spin-down bands, respectively.
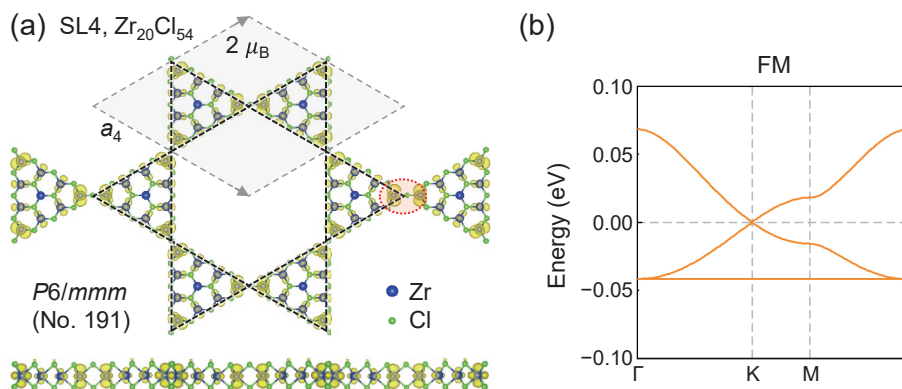
Figure 4 Atomic and electronic structure of SL4. (a) Atomic structure of SL4 (formula $Zr_{20}Cl_{54}$) with spin charge density differences ($\rho\uparrow - \rho\downarrow$) distribution. The isosurface level is chosen as 0.001 e·bohr^{-3}. The red semitransparent ellipse marks the region around a charge center. The charge centers form into an FM kagome lattice, as marked by black dashed lines. The lattice constant of SL4 (a_4) is 26.93 Å. (b) Band structure of SL4 in the FM ground state. The orange solid lines denote the spin-up bands.

To further confirm the structural stability, we carried out first-principles calculations of the phonon spectra and AIMD simulations, and constructed a convex hull diagram for these SLs, i.e., SL2, SL3, and SL4. The calculated results are summarized in Figs. S1–S3 in the Electronic Supplementary Material (ESM). Figure S1 in the ESM shows the phonon dispersions of SL2, SL3, and SL4. Very tiny imaginary frequencies (< 0.1 THz) are observed in the phonon spectra due to the limited sizes of supercells that may ignore some of the long-range force constants, indicating these SLs are dynamically stable. Figure S2 in the ESM shows the AIMD results of SLs at 300 K for 10 ps. The slight fluctuations of the free energy and atomic structure confirm the good thermodynamic stability of these SLs. From the Computational 2D Materials Database (C2DB), we found several Zr_mCl_n compounds, some of them have been reported, such as ZrCl [54], $ZrCl_2$ (bulk fabricated in Ref. [36]), and inversion-breaking $ZrCl_3$(II) [51]. We combined these structures from C2DB with our predicted SLs to obtain the convex hull diagram, as shown in Fig. S3 in the ESM. Notice SL2 (Zr_6Cl_{18}, 1:3 stoichiometric ratio) is 0.075 eV/Zr lower than $ZrCl_3$(I) and 0.368 eV/Zr lower than $ZrCl_3$(II). Thereby, $ZrCl_2$ and SL2 are chosen as the two ends of the convex hull with zero formation energy in Fig. S3 in the ESM. Besides, SL3 and SL4 are on the convex hull because they have negative formation energies and there are no other compounds with the same stoichiometric ratio reported in the literature. Given the above aspects, we now conclude that SL2, SL3, and SL4 are structurally stable in the 2D geometries and deserve experimental attention for further applications.

Last but most important, understanding the underlying mechanism of different superatomic magnetic orders is essential for future studies of superatomic magnetism. In Fig. 5, we illustrate the magnetic ground states using the simple superatom dimer. A similar physical picture can be extended into superatomic lattices if the coupling between different cells is further considered. First, one should notice that the superatom has an internal structure that its atoms are in different chemical environments. As shown in Fig. 5(a), there are three types of Zr atoms in our studied superatoms, i.e., d^1 and $d^{4/3}$ Zr atoms at boundaries, and d^2 Zr atoms in bulk. Figure 5(b) shows the crystal field splitting of different local Zr atoms, which also explains that the electronic states near the Fermi level of SL2, SL3, and SL4 are mainly composed of d_{z^2} and nearly degenerate d_{xy} and $d_{x^2-y^2}$ orbitals. Second, we discussed two key factors in forming superatomic magnetism: One is the integer superatomic spin formed by the hybridization of d orbitals of local Zr atoms, and the other is the magnetic ground state from competition between

effective inter-superatom hopping t_s and on-site repulsion U. For $N = 2$ superatom, the spin state of 1 μ_B for each superatom is from the energy level splitting, shown in gray boxes of Fig. 5(c). Given t_s between S1 and S2 is strong, which eventually forms the superatomic FM state ($t_s > U$), as illustrated in Fig. 5(c). For larger $N = 3$ and $N = 4$ superatoms, the superatomic spin of S1 (S2) from energy level splitting is much more complicated. From Haldane's conjecture [55] and our calculations in Figs. 3 and 4, we find each $N = 3$ or $N = 4$ superatom still carries an integer magnetic moment of 1 μ_B. For $N = 3$ superatom, Fig. 5(d) shows that the charge center locates in the middle part (see Fig. 3(a)). Such charge center distribution comes from the moderate size of $N = 3$ superatom that the charge density prefers to gather at $d^{4/3}$ Zr atoms. Therefore, t_s is weak due to the long distance between different charge centers, leading to an AFM coupling ($t_s < U$) in Fig. 5(d). For $N = 4$ superatom in Fig. 5(e), the existence of bulk d^2 Zr atom make it difficult for its charge density (near Fermi level) to gather in the middle part. The vertex d^1 Zr atoms are energetically favorable as the charge centers, resulting in a strong t_s ($t_s > U$) and the FM ground state.

4   Conclusions

Before closing, we would like to make some remarks on our work. First, previous studies of superatomic materials mostly focus on carbon-based systems like nanographene and its derivatives [56]. Recently, triangulene-based nanostructures with superatomic AFM order have been synthesized and attracted tremendous research interest [57, 58]. To date, however, d-orbital-based superatomic materials, especially those hosting intriguing magnetic properties, have been rarely studied. Second, our proposed superlattices have different origins of superatomic magnetism. For carbon-based superatoms, their magnetism is governed by Lieb's theorem. For our d-orbital-based superatoms, the magnetism is intrinsically from the magnetic atoms that constitute them. Therefore, our work offers an attractive platform for d-orbital-based magnetic superstructures.

In conclusion, by using first-principles calculations, we demonstrated the realization of novel 2D magnetic states based on superatomic lattices of zirconium dichloride. We found that the spin charge centers formed into different equivalent magnetic lattices in SL2, SL3, and SL4, including FM CT, AFM honeycomb, and FM kagome lattices. The various magnetic lattices originate from the geometric effect of superatomic lattices that each superatom carries an integer superatomic spin with internal distributions. By calculating the Chern numbers and electronic band structures, we found SL2 and SL4 were Chern insulators with $C = 1$, and SL3 was an AFM Dirac Mott insulator. To
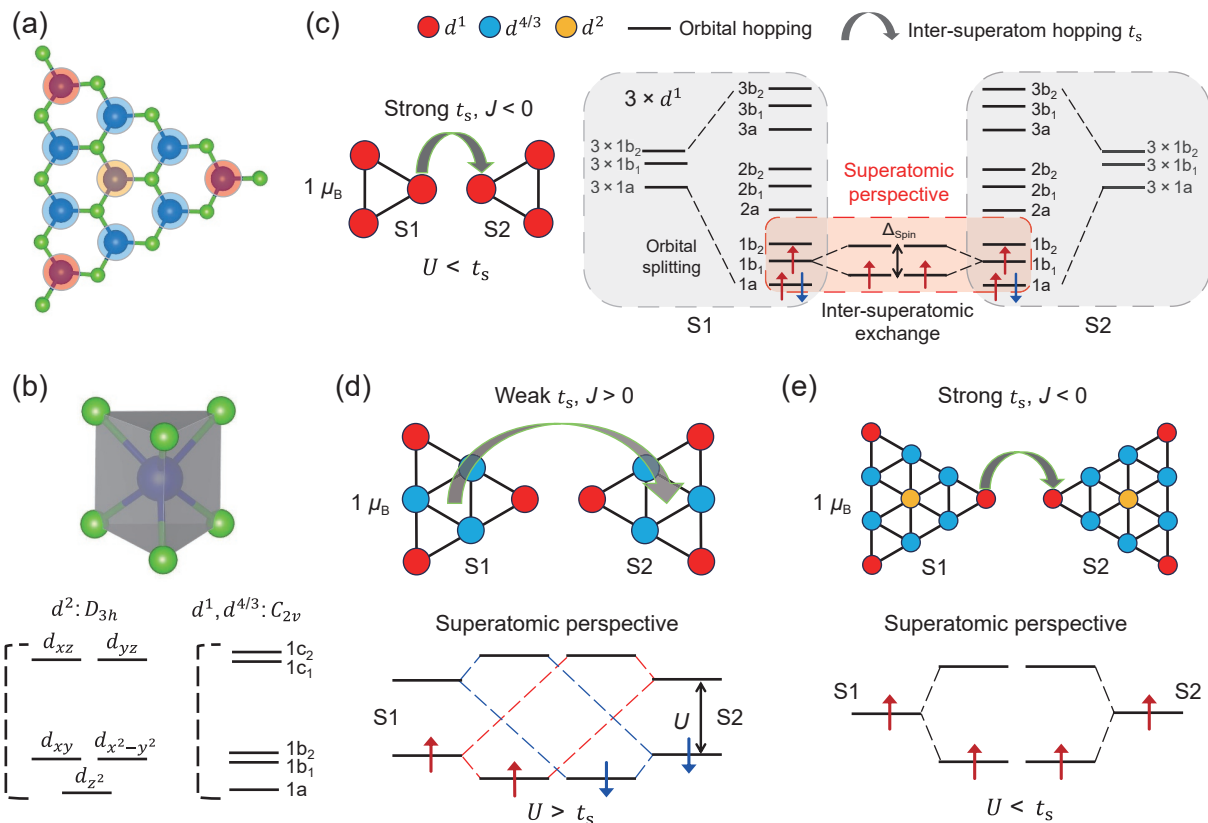
Figure 5 Magnetic ground states explained from the dimerization of superatoms. (a) Schematic diagram of one superatom with Zr atoms in different chemical environments. The boundary Zr atoms have the valence state of d^1 (red at the vertex) or $d^{4/3}$ (blue at the edge). The bulk Zr atoms have a valence state of d^2 (orange). (b) Schematic diagram of the crystal field splitting for bulk Zr atoms (D_{3h}) and boundary Zr atoms (C_{2v}). (c) Schematic diagram of the FM ground state between two $N = 2$ superatoms. Here, U denotes the effective on-site repulsion, and S1 and S2 stand for superatom 1 and superatom 2, respectively. The gray boxes of S1/S2 show the d orbital splitting due to intra-superatomic orbital hopping. The red box shows the superatomic perspective of the FM state, where S1 (S2) collectively carries a magnetic moment of 1 μ_B. (d) Schematic diagram of the AFM ground state between two $N = 3$ superatoms. Notice the upper inset shows the effective charge center locates at the middle part of S1 (S2), contributing to a weak t_s. The bottom inset shows the simplified perspective of the superatomic AFM state, where the red (blue) dotted lines link the hybridizations of superatomic up (down) spin channels. (e) Schematic diagram of the FM ground state between two $N = 4$ superatoms. The charge centers are distributed around the boundaries of S1 (S2), contributing a strong t_s.

highlight, we achieved not only the magnetic topological states but also the strongly correlated Dirac Mott insulator in a single material platform. Our work paves the way toward intriguing *d*-orbital-based superatomic magnetism and sheds light on next-generation of superatomic nanodevices.

References

[1] Mak, K. F.; Shan, J.; Ralph, D. C. Probing and controlling magnetic states in 2D layered magnetic materials. *Nat. Rev. Phys.* **2019**, *1*, 646–661.

[2] Gibertini, M.; Koperski, M.; Morpurgo, A. F.; Novoselov, K. S. Magnetic 2D materials and heterostructures. *Nat. Nanotechnol.* **2019**, *14*, 408–419.

[3] Liu, P. Z.; Williams, J. R.; Cha, J. J. Topological nanomaterials. *Nat. Rev. Mater.* **2019**, *4*, 479–496.

[4] Armitage, N. P.; Mele, E. J.; Vishwanath, A. Weyl and Dirac semimetals in three-dimensional solids. *Rev. Mod. Phys.* **2018**, *90*, 015001.

[5] Huang, B.; Clark, G.; Navarro-Moratalla, E.; Klein, D. R.; Cheng, R.; Seyler, K. L.; Zhong, D.; Schmidgall, E.; McGuire, M. A.; Cobden, D. H. et al. Layer-dependent ferromagnetism in a van der Waals crystal down to the monolayer limit. *Nature* **2017**, *546*, 270–273.

[6] Fei, Z. Y.; Huang, B.; Malinowski, P.; Wang, W. B.; Song, T. C.; Sanchez, J.; Yao, W.; Xiao, D.; Zhu, X. Y.; May, A. F. et al. Two-dimensional itinerant ferromagnetism in atomically thin Fe₃GeTe₂. *Nat. Mater.* **2018**, *17*, 778–782.

[7] Ashton, M.; Gluhovic, D.; Sinnott, S. B.; Guo, J.; Stewart, D. A.; Hennig, R. G. Two-dimensional intrinsic half-metals with large spin gaps. *Nano Lett.* **2017**, *17*, 5251–5257.

[8] Huang, B.; Clark, G.; Klein, D. R.; MacNeill, D.; Navarro-Moratalla, E.; Seyler, K. L.; Wilson, N.; McGuire, M. A.; Cobden, D. H.; Xiao, D. et al. Electrical control of 2D magnetism in bilayer CrI₃. *Nat. Nanotechnol.* **2018**, *13*, 544–548.

[9] Kane, C. L.; Mele, E. J. Quantum spin Hall effect in graphene. *Phys. Rev. Lett.* **2005**, *95*, 226801.

[10] Bernevig, B. A.; Hughes, T. L.; Zhang, S. C. Quantum spin Hall effect and topological phase transition in HgTe quantum wells. *Science* **2006**, *314*, 1757–1761.

[11] Moore, J. E. The birth of topological insulators. *Nature* **2010**, *464*, 194–198.

[12] Qi, X. L.; Zhang, S. C. Topological insulators and superconductors. *Rev. Mod. Phys.* **2011**, *83*, 1057–1110.

[13] Pesin, D.; MacDonald, A. H. Spintronics and pseudospintronics in graphene and topological insulators. *Nat. Mater.* **2012**, *11*, 409–416.

[14] Niu, C. W.; Hanke, J. P.; Buhl, P. M.; Zhang, H. B.; Plucinski, L.;

Wortmann, D.; Blügel, S.; Bihlmayer, G.; Mokrousov, Y. Mixed topological semimetals driven by orbital complexity in two-dimensional ferromagnets. *Nat. Commun.* **2019**, *10*, 3179.

[15] Niu, C. W.; Wang, H.; Mao, N.; Huang, B. B.; Mokrousov, Y.; Dai, Y. Antiferromagnetic topological insulator with nonsymmorphic protection in two dimensions. *Phys. Rev. Lett.* **2020**, *124*, 066401.

[16] Dong, W. H.; Bao, D. L.; Sun, J. T.; Liu, F.; Du, S. X. Manipulation of Dirac fermions in nanochain-structured graphene. *Chin. Phys. Lett.* **2021**, *38*, 097101.

[17] Xu, Y. F.; Elcoro, L.; Song, Z. D.; Wieder, B. J.; Vergniory, M. G.; Regnault, N.; Chen, Y. L.; Felser, C.; Bernevig, B. A. High-throughput calculations of magnetic topological materials. *Nature* **2020**, *586*, 702–707.

[18] Elcoro, L.; Wieder, B. J.; Song, Z. D.; Xu, Y. F.; Bradlyn, B.; Bernevig, B. A. Magnetic topological quantum chemistry. *Nat. Commun.* **2021**, *12*, 5965.

[19] Watanabe, H.; Po, H. C.; Vishwanath, A. Structure and topology of band structures in the 1651 magnetic space groups. *Sci. Adv.* **2018**, *4*, eaat8685.

[20] Morali, N.; Batabyal, R.; Nag, P. K.; Liu, E. K.; Xu, Q. N.; Sun, Y.; Yan, B. H.; Felser, C.; Avraham, N.; Beidenkopf, H. Fermi-arc diversity on surface terminations of the magnetic Weyl semimetal Co$_3$Sn$_2$S$_2$. *Science* **2019**, *365*, 1286–1291.

[21] Otrokov, M. M.; Klimovskikh, I. I.; Bentmann, H.; Estyunin, D.; Zeugner, A.; Aliev, Z. S.; Gaß, S.; Wolter, A. U. B.; Koroleva, A. V.; Shikin, A. M. et al. Prediction and observation of an antiferromagnetic topological insulator. *Nature* **2019**, *576*, 416–422.

[22] Noky, J.; Zhang, Y.; Gooth, J.; Felser, C.; Sun, Y. Giant anomalous Hall and Nernst effect in magnetic cubic Heusler compounds. *npj Comput. Mater.* **2020**, *6*, 77.

[23] Zhang, L. Z.; Wang, Z. F.; Huang, B.; Cui, B.; Wang, Z. M.; Du, S. X.; Gao, H. J.; Liu, F. Intrinsic two-dimensional organic topological insulators in metal-dicyanoanthracene lattices. *Nano Lett.* **2016**, *16*, 2072–2075.

[24] Li, J. H.; Wang, C.; Zhang, Z. T.; Gu, B. L.; Duan, W. H.; Xu, Y. Magnetically controllable topological quantum phase transitions in the antiferromagnetic topological insulator MnBi$_2$Te$_4$. *Phys. Rev. B* **2019**, *100*, 121103.

[25] Chang, C. Z.; Zhang, J. S.; Feng, X.; Shen, J.; Zhang, Z. C.; Guo, M. H.; Li, K.; Ou, Y. B.; Wei, P.; Wang, L. L. et al. Experimental observation of the quantum anomalous Hall effect in a magnetic topological insulator. *Science* **2013**, *340*, 167–170.

[26] Deng, Y. J.; Yu, Y. J.; Shi, M. Z.; Guo, Z. X.; Xu, Z. H.; Wang, J.; Chen, X. H.; Zhang, Y. B. Quantum anomalous Hall effect in intrinsic magnetic topological insulator MnBi$_2$Te$_4$. *Science* **2020**, *367*, 895–900.

[27] Sakai, A.; Mizuta, Y. P.; Nugroho, A. A.; Sihombing, R.; Koretsune, T.; Suzuki, M. T.; Takemori, N.; Ishii, R.; Nishio-Hamane, D.; Arita, R. et al. Giant anomalous Nernst effect and quantum-critical scaling in a ferromagnetic semimetal. *Nat. Phys.* **2018**, *14*, 1119–1124.

[28] Ghimire, N. J.; Mazin, I. I. Topology and correlations on the kagome lattice. *Nat. Mater.* **2020**, *19*, 137–138.

[29] Liu, Z.; Liu, F.; Wu, Y. S. Exotic electronic states in the world of flat bands: From theory to material. *Chin. Phys. B* **2014**, *23*, 077308.

[30] Lee, D.; Jin, K. H.; Liu, F.; Yeom, H. W. Tunable Mott Dirac and kagome bands engineered on 1T-TaS$_2$. *Nano Lett.* **2022**, *22*, 7902–7909.

[31] Paiva, T.; Scalettar, R. T.; Zheng, W.; Singh, R. R. P.; Oitmaa, J. Ground-state and finite-temperature signatures of quantum phase transitions in the half-filled Hubbard model on a honeycomb lattice. *Phys. Rev. B* **2005**, *72*, 085123.

[32] Meng, Z. Y.; Lang, T. C.; Wessel, S.; Assaad, F. F.; Muramatsu, A. Quantum spin liquid emerging in two-dimensional correlated Dirac fermions. *Nature* **2010**, *464*, 847–851.

[33] Thomas, S.; Li, H.; Bredas, J. L. Emergence of an antiferromagnetic Mott insulating phase in hexagonal π-conjugated covalent organic frameworks. *Adv. Mater.* **2019**, *31*, 1900355.

[34] Zhou, Y. N.; Liu, F. Realization of an antiferromagnetic superatomic graphene: Dirac Mott insulator and circular dichroism Hall effect. *Nano Lett.* **2021**, *21*, 230–235.

[35] Lei, L.; Dai, J. Q.; Dong, H. Y.; Geng, Y. Y.; Cao, F. Y.; Wang, C.; Xu, R.; Pang, F.; Li, F. S.; Cheng, Z. H. et al. Electronic Janus lattice and kagome-like bands in coloring-triangular MoTe$_2$ monolayers. arXiv: 2302.06166, 2023.

[36] Cisar, A.; Corbett, J. D.; Daake, R. L. The zirconium dichloride phase region. Synthesis, structure, and photoelectron spectral studies of 3R-ZrCl$_2$, 6T-Zr$_{1.05}$Cl$_2$, and related phases. *Inorg. Chem.* **1979**, *18*, 836–843.

[37] Zhang, S. H.; Kang, M.; Huang, H. Q.; Jiang, W.; Ni, X. J.; Kang, L.; Zhang, S. P.; Xu, H. X.; Liu, Z.; Liu, F. Kagome bands disguised in a coloring-triangle lattice. *Phys. Rev. B* **2019**, *99*, 100404.

[38] Kresse, G.; Hafner, J. *Ab initio* molecular dynamics for liquid metals. *Phys. Rev. B* **1993**, *47*, 558–561.

[39] Kresse, G.; Furthmüller, J. Efficiency of *ab-initio* total energy calculations for metals and semiconductors using a plane-wave basis set. *Comput. Mater. Sci.* **1996**, *6*, 15–50.

[40] Perdew, J. P.; Burke, K.; Ernzerhof, M. Generalized gradient approximation made simple. *Phys. Rev. Lett.* **1996**, *77*, 3865–3868.

[41] Monkhorst, H. J.; Pack, J. D. Special points for Brillouin-zone integrations. *Phys. Rev. B* **1976**, *13*, 5188–5192.

[42] Mostofi, A. A.; Yates, J. R.; Pizzi, G.; Lee, Y. S.; Souza, I.; Vanderbilt, D.; Marzari, N. An updated version of wannier90: A tool for obtaining maximally-localised Wannier functions. *Comput. Phys. Commun.* **2014**, *185*, 2309–2310.

[43] Sancho, M. P. L.; Sancho, J. M. L.; Sancho, J. M. L.; Rubio, J. Highly convergent schemes for the calculation of bulk and surface Green functions. *J. Phys. F Met. Phys.* **1985**, *15*, 851–858.

[44] Wu, Q. S.; Zhang, S. N.; Song, H. F.; Troyer, M.; Soluyanov, A. A. WannierTools: An open-source software package for novel topological materials. *Comput. Phys. Commun.* **2018**, *224*, 405–416.

[45] Baroni, S.; Giannozzi, P.; Testa, A. Green's-function approach to linear response in solids. *Phys. Rev. Lett.* **1987**, *58*, 1861–1864.

[46] Giannozzi, P.; de Gironcoli, S.; Pavone, P.; Baroni, S. *Ab initio* calculation of phonon dispersions in semiconductors. *Phys. Rev. B* **1991**, *43*, 7231–7242.

[47] Togo, A.; Oba, F.; Tanaka, I. First-principles calculations of the ferroelastic transition between rutile-type and CaCl$_2$-type SiO$_2$ at high pressures. *Phys. Rev. B* **2008**, *78*, 134106.

[48] Nosé, S. A unified formulation of the constant temperature molecular dynamics methods. *J. Chem. Phys.* **1984**, *81*, 511–519.

[49] Wang, V.; Tang, G.; Liu, Y. C.; Wang, R. T.; Mizuseki, H.; Kawazoe, Y.; Nara, J.; Geng, W. T. High-throughput computational screening of two-dimensional semiconductors. *J. Phys. Chem. Lett.* **2022**, *13*, 11581–11594.

[50] Mounet, N.; Gibertini, M.; Schwaller, P.; Campi, D.; Merkys, A.; Marrazzo, A.; Sohier, T.; Castelli, I. E.; Cepellotti, A.; Pizzi, G. et al. Two-dimensional materials from high-throughput computational exfoliation of experimentally known compounds. *Nat. Nanotechnol.* **2018**, *13*, 246–252.

[51] Zhang, J. Y.; Ma, C. L. Room-temperature non-Dirac quantum anomalous Hall states, half semiconductors, and strain-tuned half metals in monolayer zirconium trihalide. *Phys. Rev. B* **2021**, *104*, 205429.

[52] Wang, Z. F.; Su, N. H.; Liu, F. Prediction of a two-dimensional organic topological insulator. *Nano Lett.* **2013**, *13*, 2842–2845.

[53] Xiang, H. J.; Lee, C.; Koo, H. J.; Gong, X. G.; Whangbo, M. H. Magnetic properties and energy-mapping analysis. *Dalton Trans.* **2013**, *42*, 823–853.

[54] Dong, W. H.; Zhang, Y. Y.; Zhang, Y. F.; Sun, J. T.; Liu, F.; Du, S. X. Superconductivity and topological aspects of two-dimensional transition-metal monohalides. *npj Comput. Mater.* **2022**, *8*, 185.

[55] Haldane, F. D. M. Nonlinear field theory of large-spin heisenberg antiferromagnets: Semiclassically quantized solitons of the one-dimensional easy-axis néel state. *Phys. Rev. Lett.* **1983**, *50*, 1153–1156.

[56] Gu, Y. W.; Qiu, Z. J.; Müllen, K. Nanographenes and graphene nanoribbons as multitalents of present and future materials science. *J. Am. Chem. Soc.* **2022**, *144*, 11499–11524.

[57] Arikawa, S.; Shimizu, A.; Shiomi, D.; Sato, K.; Shintani, R. Synthesis and isolation of a kinetically stabilized crystalline triangulene. *J. Am. Chem. Soc.* **2021**, *143*, 19599–19605.

[58] Hieulle, J.; Castro, S.; Friedrich, N.; Vegliante, A.; Lara, F. R.; Sanz, S.; Rey, D.; Corso, M.; Frederiksen, T.; Pascual, J. I. et al. On-surface synthesis and collective spin excitations of a triangulene-based nanostar. *Angew. Chem., Int. Ed.* **2021**, *60*, 25224–25229.